Supplementary Material

1 LOW-ENERGY ELECTRON DIFFRACTION

Figure S1 shows the LEED patterns of WS_2 exfoliated onto Au(111) and Ag(111) by the KISS method in UHV. The Au(111) diffraction spots appear blurred and elongated compared to the Ag(111) spots due to a higher degree of the smaller grains, higher step density, and a higher degree of polycrystallinity of the Au(111) thin films, as discussed in the main text (Man et al., 2016; Haider et al., 2024). The two hexagonal patterns, rotated at different angles with respect to each other, are clearly visible, illustrating that WS_2 was successfully exfoliated using the KISS method. The angle between the WS_2 and the substrate is indicated for each flake.

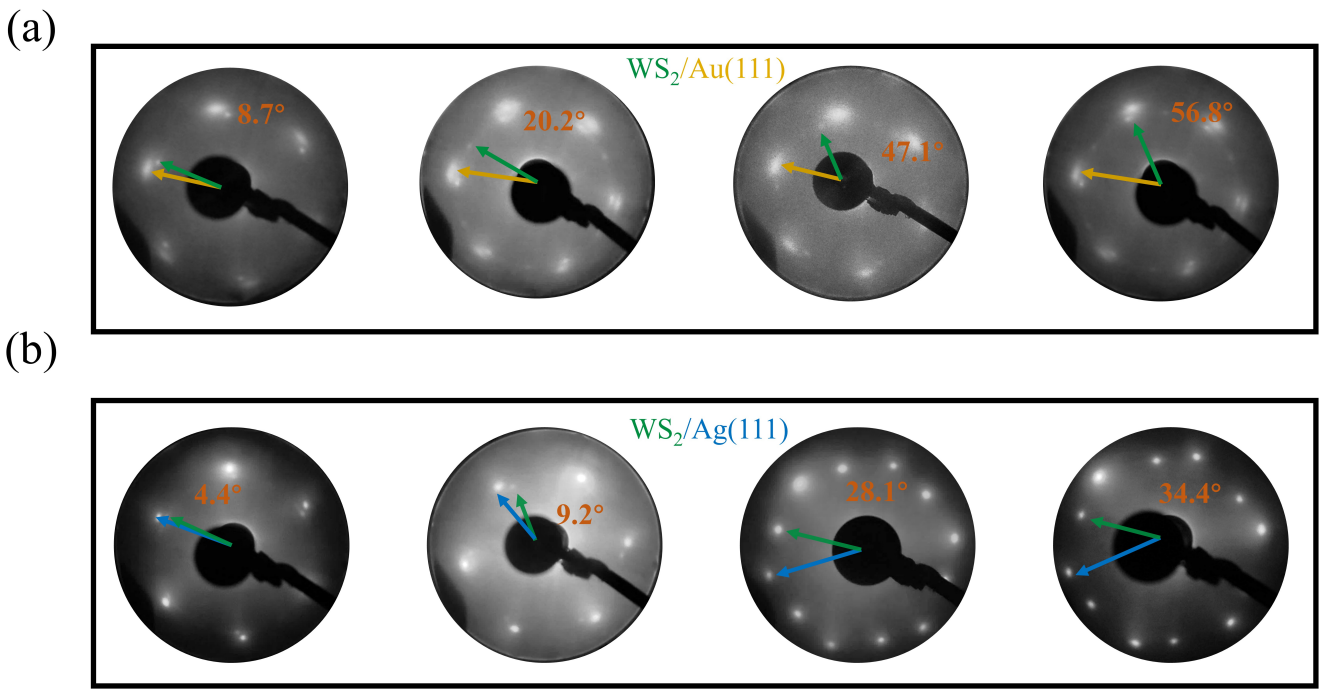

Figure S1: LEED characterization of exfoliated WS_2: LEED images of four different flakes of WS_2 on (a) Au(111) and (b) Ag(111). All images were obtained with an electron energy of 125 eV. The green arrow points to a diffraction spot of WS_2, while the yellow and blue arrows indicate the diffraction spots of Au and Ag, respectively. The angle between WS_2 and the substrate is specified for each flake.

2 OPTICAL MICROSCOPY

Figure S2 (a,b) shows representative flakes of WS_2 and **Figure S2(d,e)** WSe_2 on Au(111), along with their lateral size distribution, **Figure S2(c,f)**. The results indicate that WSe_2 is more easily exfoliated compared to WS_2.
Figure S3 presents samples exfoliated on Ag(111), where **Figure S3(a-c)** depict three WS_2 samples, and **Figure S3(d-f)** depict three WSe_2 samples.

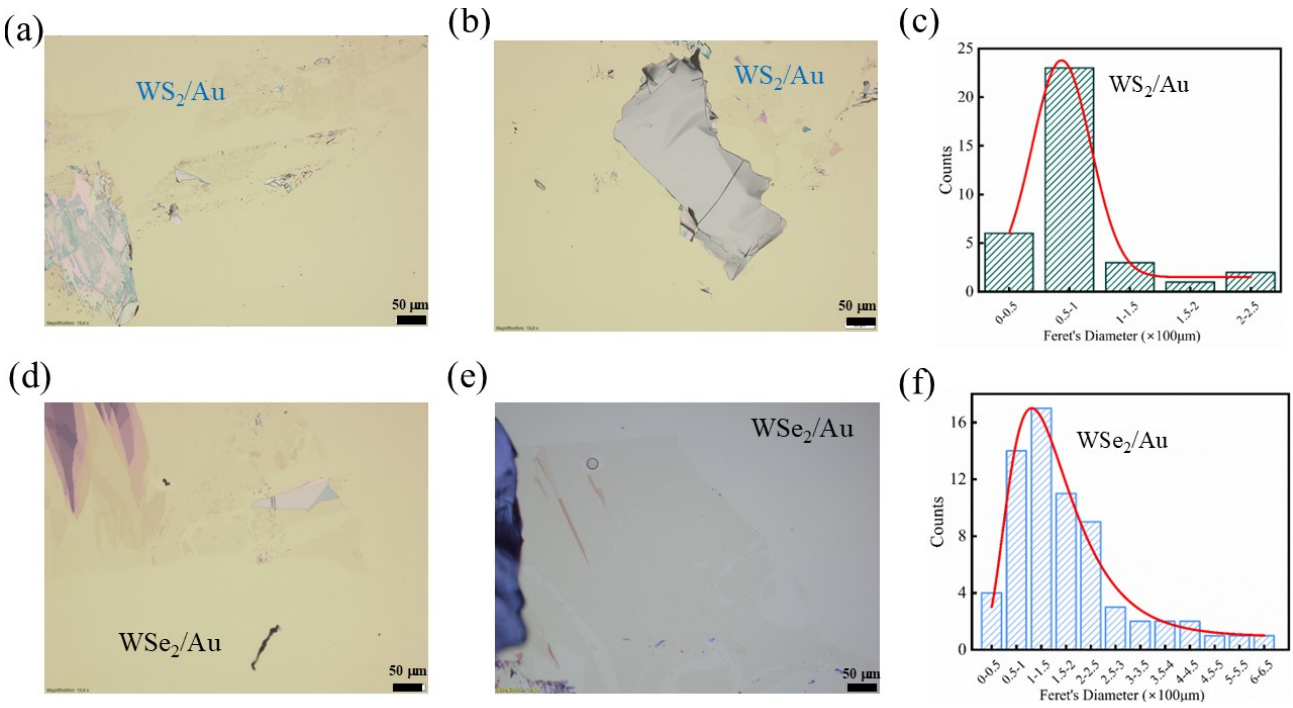

Figure S2: Optical microscopy and flake size analysis for WS_2 and WSe_2 on Au(111): (a) and (b) show two samples of WS_2 on Au(111), while (c) illustrates the lateral size distribution of the flakes. (d-f) are corresponding images for WSe_2 on Au(111).

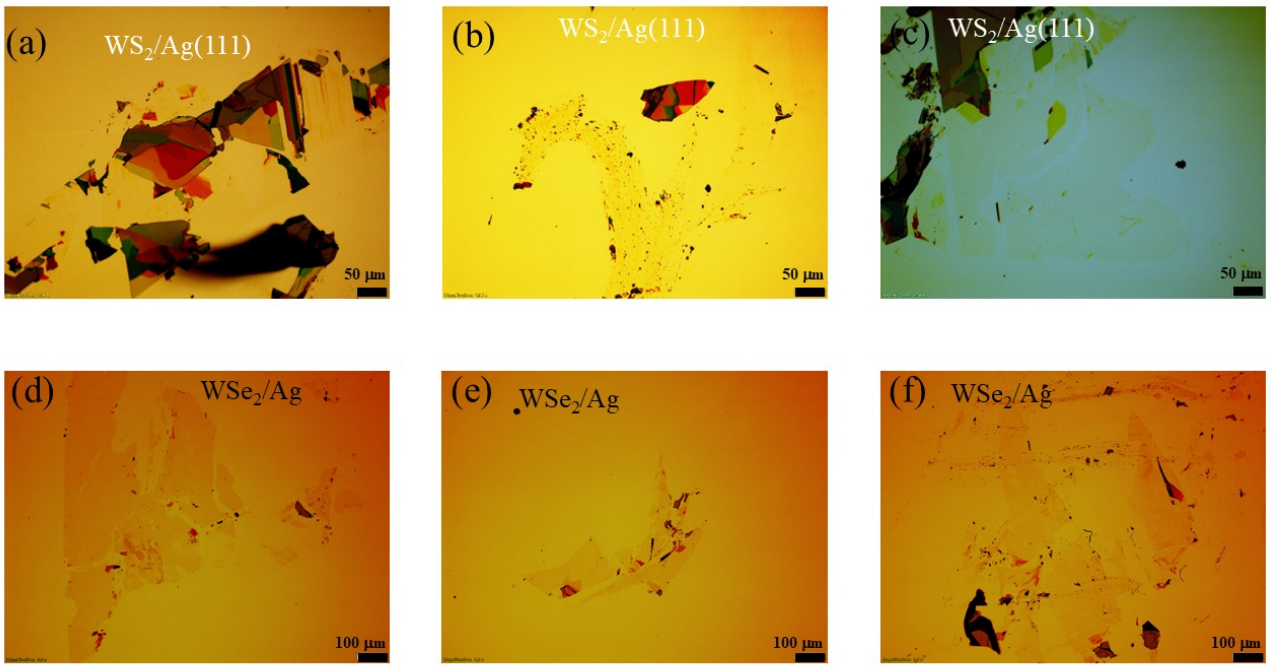

Figure S3: Optical microscopy images of WS_2 and WSe_2 on Ag(111): (a-c) show three samples of WS_2, and (d-f) show three samples of WSe_2. Color balance of the images was adjusted to make monolayers more visible.

3 X-RAY PHOTOELECTRON SPECTROSCOPY (XPS)

The XPS spectra of WS_2 on Ag(111) and Au(111) measured using a lab based spectrometer with a spot size of 1 mm^2 are shown in **Figure S4**. The characteristic peaks of the W 4*f* and S 2*p* orbitals confirm the presence of WS_2 in the sample and further indicate that the flake size meets the measurement requirements. Table S1 summarizes the binding energy values for W 4*f*, Se 3*p* and S 2*p* peaks from the XPS data presented in the main text and **Figure S4**. The data is in good agreement with values reported in the literature. Additionally, the components of oxidized W and S, expected at binding energy of 36.1 eV and 169.1 eV, respectively (Li et al., 2020), are absent, confirming the air stability of exfoliated WS_2.

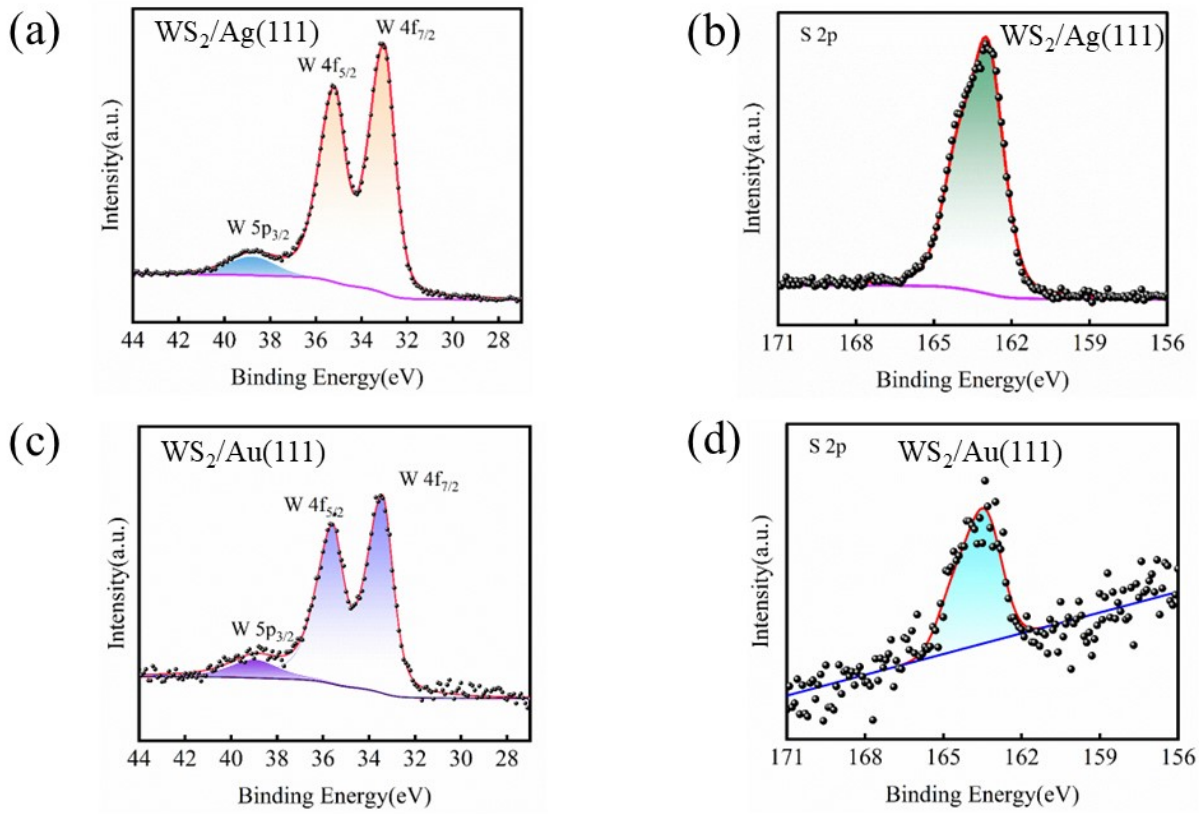

Figure S4: XPS spectra of WS_2 on Ag(111) and Au(111): Detailed scans of the (a) W 4*f* and (b) S 2*p* core level regions of WS_2/Ag(111). (c-d) detailed scans of the (c) W 4*f* and (d) S 2*p* core level regions of WS_2/Au(111).No signs of oxidation are visible for either W or S.

4 X-RAY DIFFRACTION

The single crystal X-ray diffraction measurements were performed at the I09 beamline at the Diamond Light Source (Lee and Duncan, 2018) using the UHV end-station designed for hard X-ray photoelectron spectroscopy and X-ray standing wave studies. The beam size was about 40 (H) x 20 (V) μm at the sample. After undergoing KISS exfoliation, the Ag substrate was aligned to focus the X-ray beam to a WSe_2 flake by monitoring the W 4*f* photoelectron intensity. The Ag(111) Bragg reflection was subsequently excited in

	WSe_2/Au(111) (eV)	WS_2/Au(111) (eV)	WS_2/Ag(111) (eV)
W $4f_{7/2}$	32.50	33.42	33.11
W $5p_{3/2}$	38.01	38.97	38.48
Se $3p_{3/2}$	161.21	/	/
S $2p_{3/2}$	/	163.38	162.91

Table S1. Binding energies of the core level photoemission lines for W, S and Se extracted from the spectra in Figure 5 and Figure S4. The XPS spectra were collected under the same conditions.

a near-backscattering geometry by a photon beam of 2627 eV, which was delivered by an undulator and a double-crystal Si(111) monochromator. The reflected beam was visualized by a fluorescent screen and the intensity of the beam spot was recorded by a CCD camera. **Figure S5 (d)** shows the measured Ag(111) reflectivity curve and the best fit based on dynamical theory of X-ray diffraction taking into account the contribution of the beamline optics. The FWHM of the peak was determined to be 0.95 eV, which is identical to the intrinsic width of the (111) reflection of a perfect Ag single crystal convoluted with the energy width of the Si(111) monochromator. This confirms our exfoliation process does not introduced deformation to the substrate lattice.

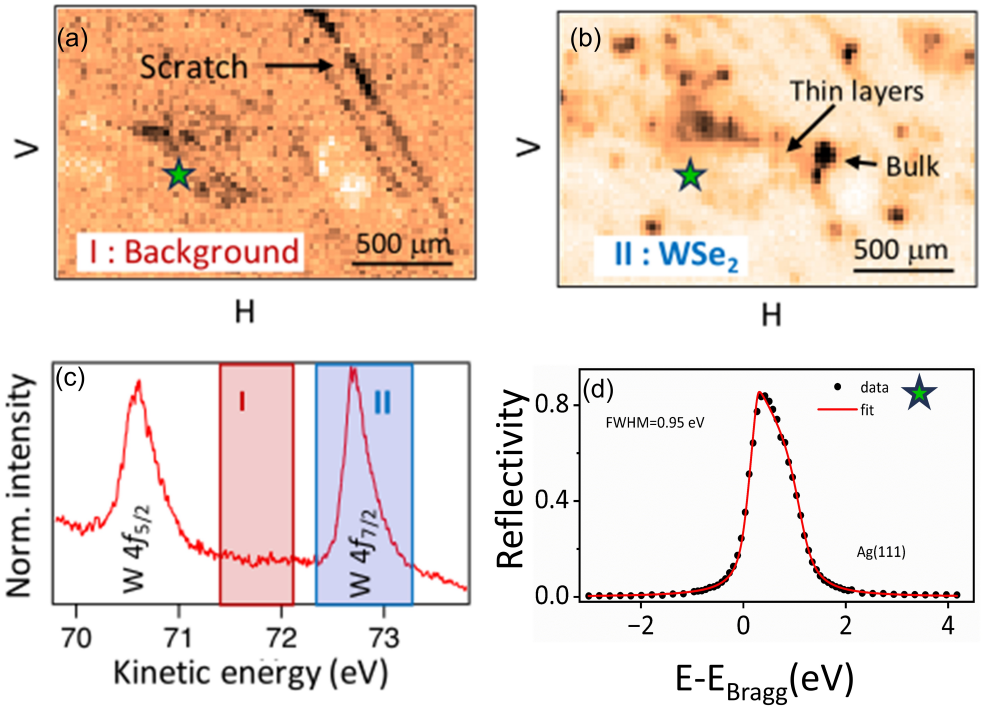

Figure S5: X-ray diffraction of WSe_2 on Ag(111): (a-b) Presents images of the background (region I) and WSe_2 flakes (region II). (c) Photoemission spectrum of the W $4f$ core level region used to select the spots marked in (a) and (b) with green stars. (d) The rocking curve of Ag(111), with FWHM = 0.95 eV.

5 BULK CRYSTAL QUALITY

The quality of the bulk crystal may also influence the success of the KISS exfoliation. **Figure S6** presents the WSe_2 and WS_2 crystals used for KISS exfoliation in this work. The WSe_2 crystal, **Figure S6(a)**, consists of two large, flat, and smooth terraces, whereas the WS_2 crystal, **Figure S6(b)**, consists of smaller grains within the larger terraces.

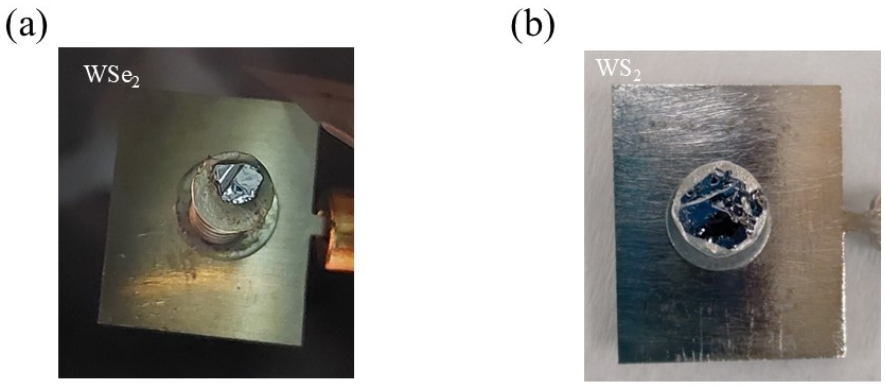

Figure S6: Images of bulk WS_2 and WSe_2 crystals: (a) bulk WSe_2 crystal with large, flat and smooth surface. (b) WS_2 bulk crystal that appears of lower quality with several smaller grains embedded in large, flat terraces.

6 SCANNING ELECTRON MICROSCOPY

The morphology of WS_2/Ag was analyzed using SEM. As shown in **Figure S7(a)**, a large and flat WS_2 flake is firmly attached to the Ag substrate. **Figures S7(b)** and **S7(c)** reveal that the Ag substrate remains smooth and intact, exhibiting no visible cracks, fractures, or deformations. Furthermore, the well-defined interface between WS_2 and the Ag substrate indicates that the KISS exfoliation process did not cause significant structural damage to the substrate or the flake.

7 KELVIN PROBE FORCE MICROSCOPY

KPFM measurements reveal a variation in the surface potential along the direction of the arrow shown in **Figure S8(a)**. The potential difference between the substrate and the WS_2 flake is determined to be 55 mV, Figure **S8(b)**. This substantial potential difference creates favorable conditions for charge transfer.

8 COMPARISON OF EXFOLIATION METHODS

To highlight the differences between different key methods used to fabricate two-dimensional materials, particularly transition-metal dichalcogenides, we present a comparison table that contrasts kinetic *in situ* single-layer synthesis (KISS), mechanical exfoliation (ME), chemical vapour deposition (CVD) and liquid phase exfoliation (LPE) based on their performance in terms of flake size, defect density, and reproducibility, as shown in Table S2.

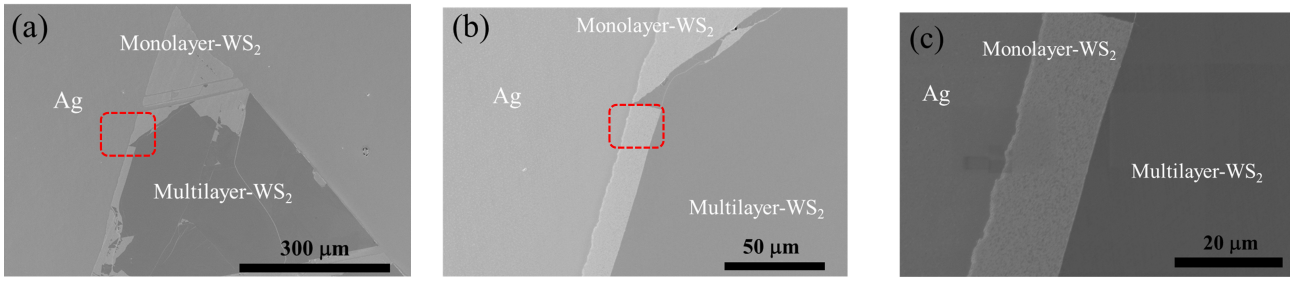

Figure S7: SEM images of WS_2/Ag. (a) A representative WS_2 flake with monolayer and multilayer regions. (b) A higher-magnification view of the region highlighted in red in (a). (c) An even higher magnification view of the area highlighted in red in (b), showing the interface region between the substrate and the flake.

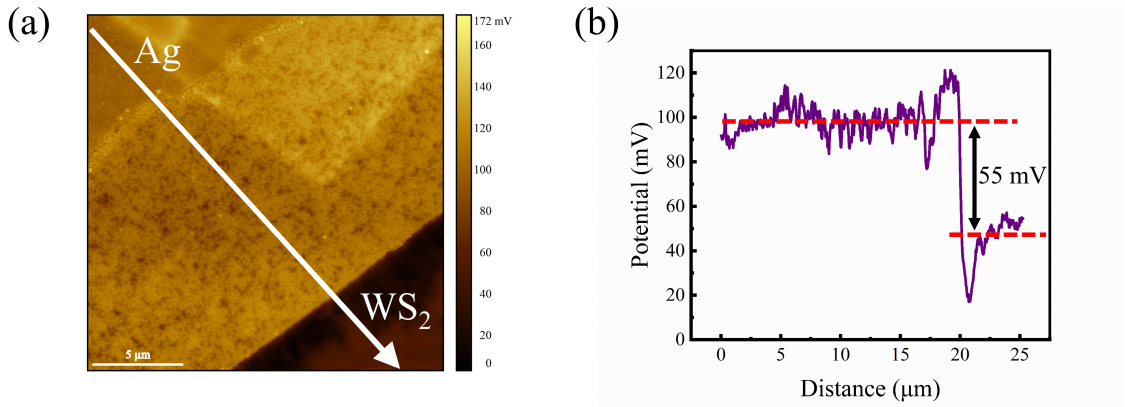

Figure S8: KPFM measurements of WS_2/Ag: (a) Micrograph showing the surface potential differences of the WS_2/Ag. (b) The potential profile along the white line in (a) from Ag to WS_2.

	Lateral Size	Reproducibility	Quality	Ref
KISS	$> 700\ \mu$m	Yes	No Air bubbles	This work
ME	$< 100\ \mu$m	Yes	Low defect density	(Islam et al., 2022)
CVD	Wafer scale	One recipe, one material	High defect density	(Kim et al., 2020)
LPE	$< 100\ \mu$m	Yes	High defect density	(Paton et al., 2014)

Table S2. Comparison of key techniques for the production of 2D TMDCs in terms of flake size, defect density and reproducibility.

REFERENCES

Haider, G., Gastaldo, M., Karim, B., Plsek, J., Varade, V., Volochanskyi, O., et al. (2024). Highly Efficient Bulk-Crystal-Sized Exfoliation of 2D Materials under Ultrahigh Vacuum. *ACS Applied Electronic Materials* 6, 2301–2308

Islam, M. A., Serles, P., Kumral, B., Demingos, P. G., Qureshi, T., Meiyazhagan, A., et al. (2022). Exfoliation mechanisms of 2d materials and their applications. *Applied Physics Reviews* 9

Kim, H.-U., Kanade, V., Kim, M., Kim, K. S., An, B.-S., Seok, H., et al. (2020). Wafer-scale and low-temperature growth of 1T-WS_2 film for efficient and stable hydrogen evolution reaction. *Small* 16, 1905000

Lee, T.-L. and Duncan, D. A. (2018). A two-color beamline for electron spectroscopies at diamond light source. *Synchrotron Radiation News* 31, 16–22

Li, G., Wang, Y., Bi, J., Huang, X., Mao, Y., Luo, L., et al. (2020). Partial oxidation strategy to synthesize WS_2/WO_3 heterostructure with enhanced adsorption performance for organic dyes: Synthesis, modelling, and mechanism. *Nanomaterials* 10, 278

Man, M. K., Deckoff-Jones, S., Winchester, A., Shi, G., Gupta, G., Mohite, A. D., et al. (2016). Protecting the properties of monolayer MoS_2 on silicon based substrates with an atomically thin buffer. *Scientific reports* 6, 20890

Paton, K. R., Varrla, E., Backes, C., Smith, R. J., Khan, U., O'Neill, A., et al. (2014). Scalable production of large quantities of defect-free few-layer graphene by shear exfoliation in liquids. *Nature materials* 13, 624–630